Inorganic Chemistry
Article
Cite This: *Inorg. Chem.* XXXX, XXX, XXX−XXX
pubs.acs.org/IC

On the Origin of the Negative Thermal Expansion Behavior of YCu

Hiroshi Mizoguchi,*[†,§] Joonho Bang,[†,§] Takeshi Inoshita,[†] Toshio Kamiya,[†,‡] and Hideo Hosono*[†,‡]

[†]Materials Research Center for Element Strategy, Tokyo Institute of Technology, 4259 Nagatsuta, Midori-ku, Yokohama 226-8503, Japan

[‡]Laboratory for Materials Research, Institute of Innovative Research, Tokyo Institute of Technology, 4259 Nagatsuta, Midori-ku, Yokohama 226-8503, Japan

Supporting Information

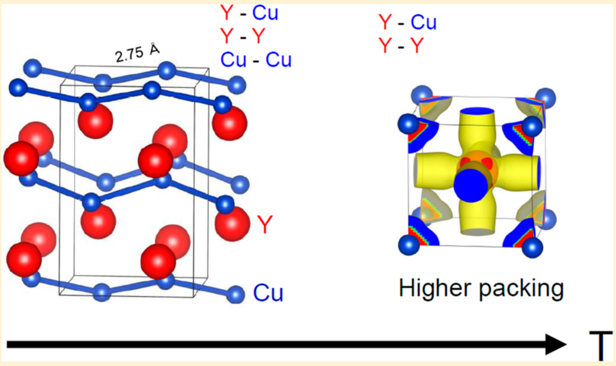

ABSTRACT: Among the intermetallics and alloys, YCu is an unusual material because it displays negative thermal expansion without spin ordering. The mechanism behind this behavior that is caused by the structural phase transition of YCu has yet to be fully understood. To gain insight into this mechanism, we experimentally examined the crystal structure of the low-temperature phase of YCu and discuss the origin of the phase transition with the aid of thermodynamics calculations. The result shows that the high-temperature (cubic CsCl-type) to low-temperature (orthorhombic FeB-type) structural phase transition is driven by the rearrangement of three covalent bonds, namely, Y−Cu, Y−Y, and Cu−Cu, which compete for the bonding energy and phonon entropy. At low temperatures, the mixing of Y and Cu does not take place easily because of the weak attractive force between these atoms expected from the small negative mixing enthalpy. This causes all three interactions to take part in the bonding, and Y and Cu are segregated to form an FeB-type structure, which is stabilized by internal energy. At higher temperatures, Cu ions are bound loosely with Y ions due to the large Y−Cu distance (3.01 Å), which results in large vibration entropy and stabilizes a CsCl-type crystal structure. In addition, the CsCl-type structure is reinforced by the Y−Y interaction between next-nearest neighbors, resulting in a smaller unit cell volume. The crystal structure has the simple cubic framework of Y containing Cu ions bound loosely at the cavity sites. The calculated frequency of the Y-like phonon modes is much higher than that of the Cu-like modes, indicating the presence of Y−Y covalent interactions in the CsCl-type phase.

INTRODUCTION

The thermal expansion of solids reflects the temperature dependences of crystal, electronic, and phonon structures. The interatomic distances in solids usually increase with temperature, resulting in positive thermal expansion due to the asymmetric shapes of interatomic potentials formed by the attractive force induced by covalent/ionic chemical bonding and the sharp repulsive force owing to the Pauli exclusion principle.[1] However, unusual materials that display zero thermal expansion (ZTE) or negative thermal expansion (NTE) are known to exist.[1] The anomalous thermal behavior often originates from magnetic ordering coupled with a negative volume change in magnetic materials, whereas large phonon entropy such as bending vibration induces such behavior in covalent bonding materials containing atoms with a low coordination number.[1] The latter inevitably occurs in low-packing-density crystal structures, whereas the former often plays a crucial role in alloys. For example, the strong correlation in metallic Fe between the magnetism and the unusual phase transition against temperature is well-known, which gives rise to a body centered cubic (bcc)−face centered cubic (fcc)−bcc sequential transition accompanying NTE.[2] These useful metallic materials, such as Invar alloys, a representative ZTE material, have been utilized practically in high precision instruments containing bimetals.

On the other hand, intermetallics (IMCs) have attracted a great deal of attention because they often exhibit various magnetic, electrical, and mechanical properties, such as the permanent magnet $SmCo_5$ and the shape memory material NiTi.[3] In IMCs, we can see the contribution of ionic or covalent bonds, as well as metallic bonds.[4] As a result, the chemical bonding of IMCs can exhibit complex temperature variations. Some IMC materials showing ZTE or NTE have been reported.[5−10] Among them, YCu and IMCs with an MgAgAs-type crystal structure are particularly noteworthy because they exhibit NTE purely due to the temperature dependence of their chemical bonds. LaNiSb or TiPtGe takes the MgAgAs-type (half Heusler-type) crystal structure, which is one of the defect bcc structures containing a vacancy site,

Received: July 5, 2019

DOI: 10.1021/acs.inorgchem.9b01988

inevitably resulting in low-packing-density crystal structures.[5−7] The annihilation of vacancy sites at high temperatures seems to be the origin of the NTE behavior in this family of materials. In contrast, the origin of the phase transition of YCu has yet to be clarified fully.[10] YCu displays a phase transition between 140 and 550 K, accompanying a structural change from the cubic CsCl-type (B2 type) to an unidentified orthorhombic structure as the temperature decreases. The low-temperature phase (LT phase) appears to adopt an orthorhombic FeB-type crystal structure (B27 type), according to theoretical studies;[11,12] however, the details of the crystal structure have not yet been experimentally clarified. Although Ritter et al. reported the crystal structure of $Y_{0.9}Tb_{0.1}Cu$, they did not report the crystal structure of pure YCu (LT),[13] probably owing to the difficulty associated with the synthesis of a fine powder (as described later, the mechanically ductile properties make the pulverization of YCu difficult). Although the unique properties of these substances are valuable, it is important to note that IMCs have certain drawbacks with respect to their practical application. Most IMCs are not mechanically ductile but brittle,[14] which prevents their practical application, even though they have the unique physical properties described above. In 2003, ductile LnCu (Ln: lanthanides or Y) IMCs with the CsCl-type crystal structure including YCu were reported by Gschneidner et al.[15] This resulted in many studies on the mechanical properties of related IMCs.[16] In this study, we report on the structural determination of YCu and details related to its phase transition, including electronic structures and the thermodynamic phase stability. Competition among Y−Cu, Y−Y, and Cu−Cu bonds exists in YCu, which exhibits the unusual thermal behavior. At higher temperatures, YCu adopts a CsCl-type crystal structure where Cu ions are loosely bound with Y ions owing to the long Y−Cu distance (3.01 Å), and its large vibration entropy stabilizes this structure at high temperatures. The CsCl-type crystal structure is reinforced by the Y−Y interaction between next-nearest neighbors, resulting in a slightly dense packing structure. The Y−Y covalent interaction causes several unusual phonon behaviors in the high temperature phase, although Y is heavier than Cu. Once cooled, the Y−Y and Cu−Cu covalent interactions take part in the bonding, and segregation in the larger unit cell forms the FeB-type crystal structure, which is stabilized by internal energy.

■ EXPERIMENTAL SECTION

The reactants were Cu (99.99%, Kojundo Kagaku, Japan), Y (99.9%), La (99.9%), Ce (99.9%), Pr (99.9%), Nd (99.9%), Sm (99.9%), Gd (99.9%), Tb (99.9%), Dy (99.9%), Ho (99.9%), Er (99.9%), and Tm (99.9%). All the Ln metals were purchased from Nippon Yttrium (Japan). LnCu was prepared from a stoichiometric mixture of Cu and Ln via arc melting on a water-cooled Cu hearth in a high-purity Ar atmosphere. To obtain homogeneous samples, the melting process was repeated several times. Annealing at 723 K for 50−150 h in an evacuated silica ampule was carried out for LnCu (Ln = La, Ce, Pr, or Nd) samples, because they melt incongruently. The Ln/Cu ratios were determined using an electron probe microanalyzer (EPMA, JEOL model JXA-8530F). The crystal structures of the synthesized materials were examined by powder X-ray diffraction (XRD; Bruker D8 Advance) using Cu K_α radiation with the aid of Rietveld refinement using the TOPAS4 code.[17] XRD data were collected in the range $2\theta = 20{-}130°$ at 0.02° intervals at room temperature. To determine the lattice constants in the temperature range of 300−723 K, XRD data were collected using a Philips X'Pert-MPD-OES X-ray powder diffractometer. For powder XRD measurements, a powder was obtained by crushing in liquid N_2 at a temperature below the ductile−brittle transition temperature (DBTT, ∼100 K),[16b] as the pulverization of a ductile YCu sample is difficult at higher temperatures. To obtain fine powders, a planetary ball mill was used at a rotation speed of 300 rpm. The temperature dependence of electrical resistivity was measured over a temperature range of 2−310 K using the conventional four-probe method. A vibrating sample magnetometer (Quantum Design, PPMS, VSM) was used for the magnetization measurements of bulk samples.

Density functional theory (DFT) calculations were performed using the generalized gradient approximation (GGA) with the Perdew−Burke−Ernzerhof (PBE) functional and the projector augmented plane-wave method implemented in the Vienna *ab initio* simulation program (VASP) code.[18] The 4s, 4p, 4d, and 5s electrons of Y and the 3d, 4s, and 4p electrons of Cu were used as valence electrons. The plane-wave-basis cutoff energy was set to 600 eV. Structural relaxations were performed using 8 × 8 × 8 and 4 × 6 × 6 *k*-point meshes for the high- and low-temperature structures of YCu until the Hellmann−Feynman forces were less than 10^{-8} eV Å^{-1}. The $4a \times 4b \times 4c$ (128 atoms) and $2a \times 3b \times 2c$ (96 atoms) supercells were respectively constructed for the high and low temperature structures of YCu to calculate the phonon thermodynamics and Cu-displacement-dependent total energy. For the supercells, a 6 × 6 × 6 *k*-point mesh was used. For the analysis of chemical bonding, the crystal orbital Hamilton population (COHP) was calculated using the local-orbital basis suite toward electronic structure (LOBSTER).[19] The atomic charges were estimated from a Bader charge analysis,[20] and the crystal structures and electron isosurfaces were visualized with the VESTA code.[21]

The phonon frequencies and eigenvectors were determined using the frozen phonon approach[22] as implemented in the Phonopy code.[23] After the normal modes were identified, the Helmholtz energy F was approximated using the following equations:

$$F(V, T) = E_0(V) + F_{\text{phonon}}(V, T) + F_{\text{electron}}(V, T)$$

where E_0 is the total energy at 0 K obtained by the DFT calculations, and F_{phonon} and F_{electron} are the phonon and thermal electronic contributions to the Helmholtz energy, respectively. The phonon contribution is expressed as

$$F_{\text{phonon}} = \frac{1}{2}\sum_{\boldsymbol{q},\nu} \hbar\omega_{\boldsymbol{q},\nu} + k_B T \sum_{\boldsymbol{q},\nu} \ln[1 - e^{-\hbar\omega_{\boldsymbol{q},\nu}/k_B T}]$$

where $\boldsymbol{q}$ and ν are the wave vector and band index, respectively, and $\hbar$ is the reduced Planck constant. The variable $\omega_{\boldsymbol{q},\nu}$ is the phonon angular frequency at $\boldsymbol{q}$ and ν; k_B is the Boltzmann constant, and T is the temperature. The thermal electronic contribution is given by

$$F_{\text{electron}} = E_{\text{electron}} - TS_{\text{electron}}$$

where E_{electron} and S_{electron} are the thermal internal energy and the entropy contribution, respectively. The thermal internal energy due to electron excitation is given by

$$E_{\text{electron}} = \int_0^\infty n(\varepsilon) f\varepsilon \, d\varepsilon - \int_0^{\varepsilon_F} n(\varepsilon)\varepsilon \, d\varepsilon$$

where $n(\varepsilon)$ is the electronic density of states, f is the Fermi−Dirac distribution, and ε_F is the Fermi energy. The variable ε_F is determined by the charge neutral condition at the given temperature. The electronic entropy is given by

$$S_{\text{electron}} = -k_B \int n(\varepsilon)[f \ln f + (1 - f)\ln(1 - f)] \, d\varepsilon$$

To obtain precise phonon dispersions, $4a \times 4b \times 4c$ (128 atoms) and $2a \times 3b \times 2c$ (96 atoms) supercells were used for the high- and low-temperature structures of YCu, respectively, and an atomic displacement of 0.01 Å was chosen.

DOI: 10.1021/acs.inorgchem.9b01988
Inorg. Chem. XXXX, XXX, XXX−XXX

Table 1. Selected Distances and Angles for LnCu Compounds Adopting the FeB-Type Crystal Structure (Ln = La, Ce, Pr, Nd, Sm, and Y)

compound	Ln−Cu distances (Å)	Ln−Ln distances (Å)	Cu−Cu distances (Å)	Cu−Cu−Cu angle (deg)
LaCu	2.961(8), 3.035(8), 2 × 3.077(4), 3.178(6), 2 × 3.285(2)	2 × 3.752(3), 4 × 3.853(3), 2 × 4.074(4)	2 × 2.772(5)	112.7(2)
CeCu	2.976(7), 3.015(7), 3.056(5), 2 × 3.080(3), 2 × 3.191(5)	2 × 3.731(3), 4 × 3.803(3), 2 × 3.996(4)	2 × 2.725(5)	114.0(3)
PrCu	2.969(5), 2.981(6), 3.037(6), 2 × 3.093(3), 2 × 3.132(4)	4 × 3.770(2), 2 × 3.773(2), 2 × 3.942(3)	2 × 2.707(4)	114.8(2)
NdCu	2.899(7), 2.947(6), 3.059(7), 2 × 3.065(4), 2 × 3.160(4)	4 × 3.749(3), 2 × 3.761(3), 2 × 3.918(4)	2 × 2.657(5)	118.1(2)
SmCu	2.788(9), 3.037(6), 2 × 2.990(4), 3.040(9), 2 × 3.132(5)	4 × 3.728(3), 2 × 3.737(3), 2 × 3.820(4)	2 × 2.694(6)	114.4(3)
YCu	2.796(9), 2.924(9), 2 × 2.972(3), 2 × 3.027(5), 3.057(7)	4 × 3.684(5), 2 × 3.691(5), 2 × 3.746(6)	2 × 2.748(7)	109.5(3)

■ RESULTS AND DISCUSSION

Synthesis and Structure Refinements. Powder XRD measurements confirmed that the gold-colored LnCu samples (Ln = Y, Gd−Tm) take a cubic CsCl-type crystal structure at 300 K, which is consistent with previous research.[24] The other gold-colored LnCu samples (Ln = La−Sm) take the orthorhombic FeB-type crystal structure at 300 K. X-ray Rietveld structure refinements were performed for LnCu (Ln = La, Ce, Pr, Nd, and Sm). Table S1 and Figure S1 in the Supporting Information provide the refinement results. Some bond distances and angles are given in Table 1.

Hereafter, we specifically focus on YCu. The low-temperature phase of YCu (LT YCu) was synthesized by cooling of the high-temperature phase of YCu (HT YCu) into 77 K. It coexists together with HT YCu, owing to the low transformation rate of the structural transition at low temperatures. The mixture of YCu polymorphisms was refined using multiphase Rietveld structure refinements (Figure S1f). Figure 1c shows the structure of HT YCu, and Table 2 provides some bond distances. The CsCl-type structure with the space group $Pm\bar{3}m$ (no. 221) is an ordered phase with the bcc-type structure. In the IMC, each metallic atom traces out a simple cubic (SC) framework. The numbers of Y−Cu, Y−Y, and Cu−Cu bonds per formula unit are summarized in Table 3.

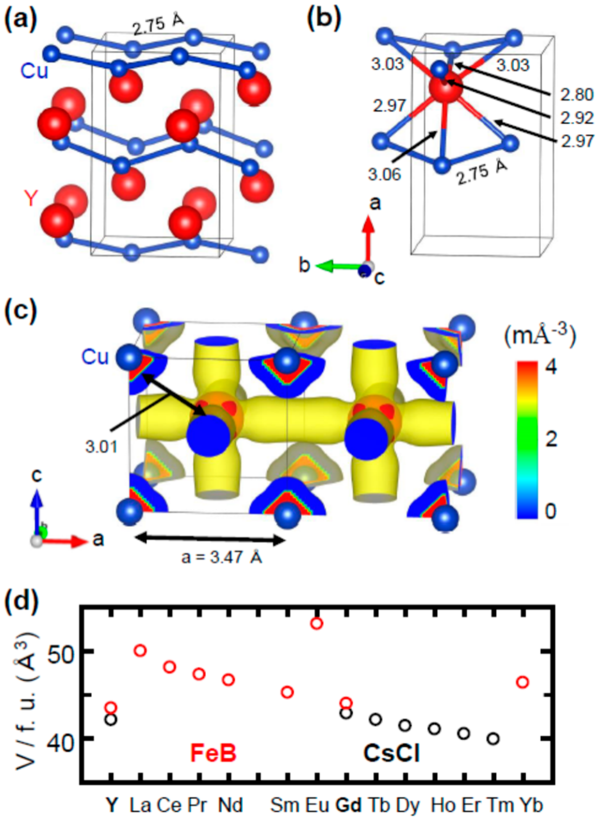

Figure 1. (a) Crystal structure of LT YCu (FeB-type structure) and (b) coordination structure around Y. (c) Crystal structure of HT YCu (CsCl-type structure). An electron density isosurface map plotted at 0.4 mA^{-3} near the Fermi energy (E_F) is superimposed. (d) Variation of unit cell volume for the LnCu family. The volumes of EuCu and YbCu are taken from the literature.[26,27]

Table 2. Selected Distances for YCu (HT, CsCl-Type) with Cubic Lattice Constant a = 3.4740(2) Å and a Unit Cell Volume of 41.925(7) Å^3

Y−Cu distance (Å)	Cu−Cu distance (Å)	Y−Y distance (Å)
8 × 3.009	6 × 3.474	6 × 3.474

It is noted that the number of Y−Y bonds per formula unit is three, whereas the Y ion coordinates with six nearest neighbors. From the viewpoint of the bond number, the Y−Cu bond seems to be dominant, whereas the Y−Cu distance (3.01 Å) is not so short. For LT YCu, the powder XRD patterns are indexed as orthorhombic cells, which is consistent with the preceding prediction by DFT structure relaxation calculations.[11,12] The crystal structure of LT YCu was refined based on the orthorhombic FeB-type structure with the space group *Pnma* (no. 62) (Figure S1f), and the obtained structure is shown in Figure 1a. The estimated amounts of HT YCu and LT YCu were determined to be 40 and 60 mol %, respectively. As Figure S1 shows, the crystallinity of the LnCu samples (FeB-type) degraded with decreasing Ln radius (particularly for Sm and Y). Thus, the crystal structure was also confirmed by DFT structure relaxation calculations. The calculated structure parameters are also provided in Table S1 in the Supporting Information together with experimental results, showing reasonable agreement within the standard error of the GGA PBE functional (usually the error is <2% for the lattice parameter, whereas the present error is <1% for the volume). The parameters also agree with previous theoretical data,[11] except for the values reported by Li et al.[12] In the LT structure (Figure 1a and b), the Y ion is surrounded by seven Cu ions in a distorted polyhedron, whereas the Cu ion is coordinated by two Cu ions and seven Y ions (Table 1). The symmetry of each site where an Y ion and three Cu ions are located on the same mirror plane perpendicular to the *b*-axis is C_s, as shown in

Table 3. Number of Bonds Per Formula Unit for Each Compound[a]

compound	Y−Cu	Y−Y	Cu−Cu	total
FeB-type YCu	3.5	4	1	8.5
CsCl-type YCu	8	3	3	14

[a] Here, we count the bonds (coordination numbers) within 4 Å of the central atom.

Figure 1b. We can find a Cu−Cu zigzag chain running along the *b*-axis, whereas the Cu−Cu distance (2.75 Å) is longer than that in metal Cu with a fcc type structure (2.56 Å),[25] which is indicative of a weak Cu−Cu interaction in LT YCu, where Cu and Y are separated by 2.8−3.1 Å. As shown in Table 1, the Cu−Cu distances for the FeB-type LnCu (Ln = La, Ce, Pr, Nd, Sm, or Y; 2.66−2.77 Å) are longer than those for Ln = Eu or Yb (2.52, 2.62 Å),[26,27] indicating that the distance depends on the valence state of Ln, because Eu or Yb often favors a smaller valence state. The numbers of Y−Cu, Y−Y, and Cu−Cu bonds per f.u. are 3.5, 4, and 1, respectively, when we count the bonds within 4 Å of the central atom, and are summarized in Table 3. Notably, the number of Y−Cu bonds in LT YCu is much less than that in HT YCu. Figure S2 in the Supporting Information shows the temperature variation of the unit cell volume for YCu powder in the temperature range of 300−723 K. Both phases coexisted at low temperatures owing to the large hysteresis, and the phase transition from LT YCu to HT YCu was observed at ∼650 K. The calculated average unit cell volume in Figure S2c (blue line) exhibited NTE behavior clearly. Figure 1d presents the unit cell volumes at 300 K for the entire family of LnCu compounds. From these volumes, the trends of the crystal structures can be obtained. For larger or smaller Ln radii, the FeB-type or CsCl-type structure appears, respectively. The unit cell volumes change monotonically with the atomic number of the Ln ion in accordance with the lanthanide contraction rule, suggesting that each Ln ion adopts a similar valence state in each group, except for EuCu and YbCu. In the boundary region (Ln = Y or Gd), both crystal structures appear. Because the unit cell volume for the FeB-type is larger than that of the CsCl-type, NTE behavior emerges. The volume change in YCu is ∼4%, and the NTE behavior is accompanied by a large temperature hysteresis from direct thermal expansion measurements, as reported in the literature.[10] On heating up to 623 K, HT YCu recovered easily with a moderate transformation rate. Although the crystal structures of LT YCu (Figure 1a) and HT YCu (Figure 1c) appear very different, some researchers have suggested that YCu exhibits a martensitic transformation, which has been speculated from the shape of the hysteresis.[28] These structures seem to be tied by crystallographic shearing, as observed frequently in the martensitic transition of the shape memory material NiTi with the CsCl-type crystal structure at higher temperatures.[29]

Physical Properties. Figure 2(a, b) shows the temperature dependences of the electrical resistivity (ρ) and magnetic susceptibility (χ) of YCu rods between 2 and 310 K, respectively. Our results indicate that ρ of YCu is on the order of 10^{-2} mΩ cm at 300 K and decreases with decreasing temperature, showing a metallic behavior. On cooling, it tends to increase slightly at ∼140 K, indicating the onset of the HT−LT structural phase transition. This behavior is similar to that in a previous report.[10a] After heating, ρ did not return to its initial value at least up to 310 K. The χ−T behavior shows Pauli paramagnetic (PM) behavior, and it exhibits the onset behavior of structural phase transition and hysteresis similar to those observed in the ρ−T characteristic. The huge hysteresis value observed in our research is a characteristic of first-order phase transition.

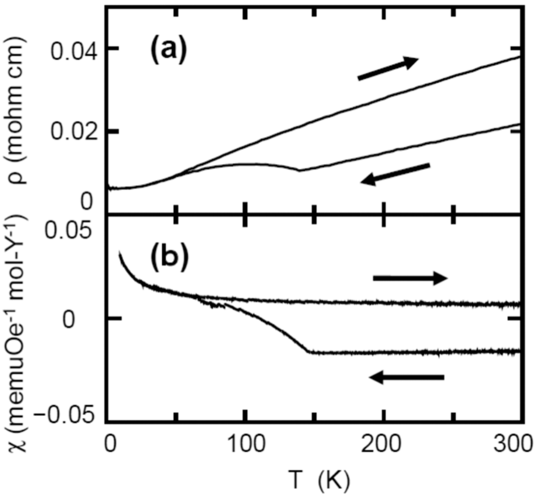

Figure 2. Temperature dependences of (a) electrical resistivity (ρ) and (b) magnetic susceptibility (χ) of YCu rods.

Electronic Structure. To obtain a deeper insight into the phase transition of YCu, we investigated the electronic structures of both HT and LT YCu phases from the perspective of chemical bonding. Figure 3a shows the E−k diagram of HT YCu. Figure S3 in the Supporting Information shows the Brillouin zone. Figure 3b and 3c show the density of states (DOS)/COHP of HT and LT YCu, respectively. The projected DOS of each atom of HT YCu is also shown in Figure S3. For our purpose, we again confirm the number of bonds per formula unit for each compound, summarized in Table 3. The smaller total number of bonds (8.5/f.u.) for the LT YCu suggests the importance of covalent interactions, which is consistent with our expectation that ionicity is lower in the FeB-type structure than in the CsCl-type structure. The calculated Bader charges for LT and HT YCu, $Y^{+1.3}Cu^{-1.3}$, agree and indicate that the difference in charge transfer between these structures is negligible, which is in agreement with the reported spectroscopic measurements.[30] Therefore,

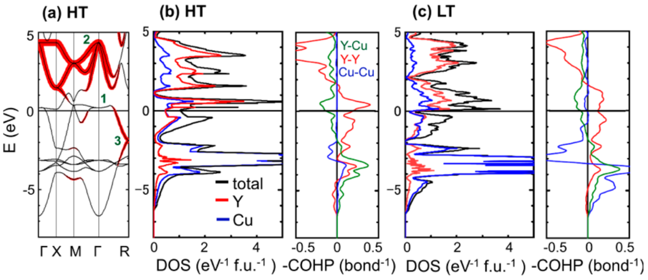

Figure 3. (a) Calculated band structure and (b) projected DOS and −COHP for HT YCu. (c) Projected DOS and −COHP for LT YCu. The energy scale is defined so that E_F corresponds to zero energy. The fatband diagram in the E−k diagram shows the contribution from Y 4d t_{2g} orbitals in red. The Brillouin zone for HT YCu is shown in Figure S3 in the Supporting Information. Regarding the Y−Y and Y−Cu interactions, the COHP curves only for the shortest distance are shown for LT YCu.

DOI: 10.1021/acs.inorgchem.9b01988
Inorg. Chem. XXXX, XXX, XXX−XXX

Table 4. Comparison of Energy Terms between FeB- and CsCl-Type Structures for YCu[c]

compound	E_{total} (eV/f.u.)	$E_{Madelung}$ (eV/f.u.)[a]	−ICOHP total (eV/f.u.)[b]	−ICOHP Y−Cu (eV/f.u.)[b]	−ICOHP Y−Y (eV/f.u.)[b]	−ICOHP Cu−Cu (eV/f.u.)
FeB-type YCu	−10.666	−8.07 ($Y^{1+}Cu^{1-}$)	5.88 (100%)	2.40 (40.7%)	3.27 (55.7%)	0.21 (3.6%)
CsCl-type YCu	−10.625	−8.44 ($Y^{1+}Cu^{1-}$)	8.54 (100%)	0.67 × 8 = 5.36 (62.8%)	1.06 × 3 = 3.18 (37.2%)	0.00 (0%)

[a] The formal charges were selected on the basis of the calculated Bader charge, $Y^{+1.3}Cu^{-1.3}$. [b] ICOHP was evaluated by taking into consideration the coordination number of each ion. [c] The Madelung energy and ICOHP as integrated up to E_F are also shown for evaluation of the ionic bonding and covalent bonding, respectively.

we do not need to consider the change in the Y/Cu size ratio during the phase transition, although this ratio is an important factor controlling the crystal structure, as shown in Figure 1d. To evaluate the ionic and covalent bond contributions, we calculated the total energies of LT and HT YCu and summarize them in Table 4, together with the Madelung energies ($E_{Madelung}$) and −ICOHP integrated to E_F (= 0 eV, Fermi energy).

The total energies (internal energies) indicate that the FeB-type structure is more energetically stable at 0 K, which agrees with experimental results. We calculated $E_{Madelung}$ using the Fourier method[21] on the basis of the results of the Bader charge calculations. The obtained $E_{Madelung}$ favors a CsCl-type structure (calculations using the same unit cell volume/f.u. of these structures indicated the same tendency). Therefore, it is evident that covalent and/or metallic interactions stabilize the FeB-type structure at 0 K. Table 4 also shows the partitioning of the covalent interactions through −ICOHP into Y−Cu, Y−Y, and Cu−Cu components. The data indicate a tendency for the fraction of −ICOHP to correspond primarily to the number of each bond (the Cu−Cu interaction of HT YCu is an exception). Although the contribution of the Y−Cu interaction (63%) is dominant for the CsCl-type, this contribution is not large despite the large number of Y−Cu bonds. This indicates that the Y−Cu interaction per bond (0.67 eV) is much weaker than the Y−Y interaction per bond (1.06 eV), reflecting the long Y−Cu distance (3.01 Å) and short Y−Y distance (3.47 Å) for the CsCl-type structure. In the FeB-type structure, the Y−Y (56%) and Cu−Cu (4%) homolytic interactions have large contributions, exhibiting high covalency (unlike the CsCl-type structure). This suggests the importance of rearrangement among the three interactions, which may dominate the structural phase transition.

Here, we explain electronic structure of HT YCu in detail. Most of the features of the calculated band structure and DOS are in fairly good agreement with previously reported results.[11,31] The $E-k$ diagram of the CsCl-type structure is derived from the band folding of the bcc lattice. The Y−Y COHP of HT YCu (Figure 3b, red line) shows Y−Y bonding interactions in the −4.4 eV to E_F region. Although the Cu−Cu distance (3.47 Å) is the same as the Y−Y distance in the CsCl-type structure, the Cu−Cu ICOHP (blue line) shows a nonbonding interaction (0%) owing to the smaller size of Cu. Figure 4b shows the electron density map in the −7.0 eV to E_F energy region on the (110) plane in HT YCu, also indicating the Cu−Cu nonbonding state. On the other hand, the Y−Cu COHP (green line) shows a bonding interaction in the −5.6 to −1.9 eV region with the sign changing at −1.6 eV. Thus, the most optimal of the three COHPs is realized at E_F, suggesting the importance of the Y−Y interaction in HT YCu. To confirm the participation of Y−Y bonding in chemical bonds, Figure 1c shows the electron density map of HT YCu in the energy region from −0.1 eV to E_F. Notably, the electron density near E_F shows a strong Y−Y interaction to form the simple cubic (SC) sublattice of Y. The Y−Y distance (3.47 Å) is slightly shorter than those (3.56 and 3.65 Å) in metal Y with an hcp structure.[32] Although the metal−metal interaction also appears in bcc metals,[4a] the widely spread Y 4d orbitals in HT YCu enhance the Y−Y interaction. The CsCl-type structure, having eight Y−Cu weak bonds per f.u., is reinforced by the Y−Y interaction, resulting in the smaller unit cell volume of HT YCu. To understand the unique chemical bonding appearing in HT YCu, we needed to delve deeper into the results of the band calculations. It is useful to pinpoint the bonding interactions that control the electronic structure. We focused on the three $E(k)$ points in Figure 3a, the orbital interactions of which are shown in Figure 4a. The fatband diagram in the $E-k$ diagram in Figure 3a also shows the orbital contribution of Y 4d t_{2g} orbitals, which are highlighted in red. Two bands originating mostly from Y 4d cross E_F, which is indicative of metallic behavior. The relatively large DOS at E_F, 1.2 eV^{-1} $f.u.^{-1}$, is indicative of Pauli PM behavior, which is consistent with the observed $\chi-T$ characteristic in Figure 2b. The occupied states are based on the Cu s−Y s σ bonding interaction (Γ, −6.7 eV) and contribute to the metallic character together with Y 4d orbitals. Cu 3d orbitals are located primarily in the narrow energy region from −2.7 to −3.5 eV, producing large DOS values. On the other hand, the bottom of the Y 4d bands dominates the DOS near E_F, together with the Cu 4p states. The Y 4d orbitals are located just above E_F and form widely spread empty conduction bands via the Y d−Y d interaction. To confirm the unique participation of Y 4d orbitals in the chemical bonding, we

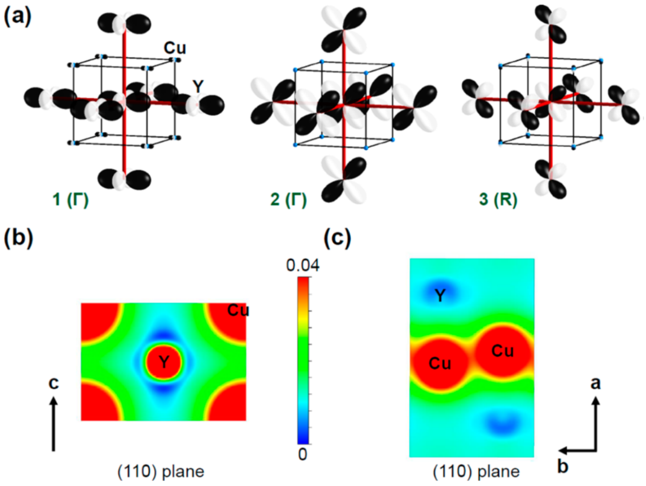

Figure 4. (a) Illustration of the orbital interactions at points 1−3 indicated in Figure 3a. Projection of the DFT pseudo-wave functions at the atomic positions in black and white indicating the relative signs of the wave function. Electron density maps in the energy region of −7 to 0 eV on the (110) plane in HT YCu (b) and the (001) plane in LT YCu (c).

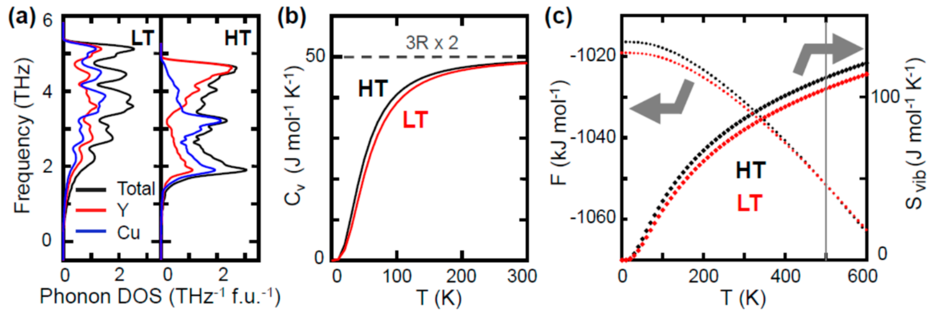

Figure 5. (a) Calculated phonon DOS of YCu. (b) Temperature dependences of calculated constant-volume heat capacity (C_v) for LT YCu (red) and HT YCu (black). (c) Temperature dependences of Helmholtz energy (F) and vibrational entropy (S_{vib}).

observe the band dispersion along Γ to R, which indicates how the orbital interaction changes when the phase relationship changes only along the <111> direction from in-phase (Γ) to opposite-phase (R) between the neighboring unit cells along the direction. For this purpose, we need to consider the periodic modulation of Bloch functions in crystalline solids.[33] Doubly degenerate Y e_g bands are located at +0.2 eV at the Γ point (point 1) owing to the direct d−d σ bonding interaction resulting from the symmetric profile of e_g orbitals, as shown in Figure 4a. When the k vector is (0, 0, 0) at the Γ point, the phase of the Bloch functions in the E−k diagram is invariant from one unit cell to another. As a result, triple degeneration of the Y t_{2g} bands located at +4.4 eV occurs at the Γ point (point 2) owing to the direct d−d π* antibonding interaction resulting from the symmetric profile of t_{2g} orbitals. As one moves to the R point, the t_{2g} bands move down to the occupied region, −1.8 eV (point 3), owing to the direct d−d π bonding interaction. At the R point (k = (1/2, 1/2, 1/2)), the phase of the basis set is inverted every time a translation of one unit cell is applied along the a, b, and c directions. One of the three states at the R point is shown in Figure 4a, and the phase variation can be seen clearly. As a result, the bottom of the Y 4d band is slightly occupied.

Next, we describe the electronic structure of FeB-type YCu. In the DOS of LT YCu (Figure 3c), the formation of a pseudo gap at E_F can be seen, where DOS(E_F) decreases to 0.5 eV^{-1} f.u.$^{-1}$. The E−k diagram of LT YCu is shown in Figure S4 in the Supporting Information. As shown by red circles, many avoided crossings occur around E_F, probably owing to the crystallographic symmetry lowering. This is the origin of the pseudo gap at DOS(E_F). The pseudo gap suggests that the electrical resistivity increases, which may explain the experimental results obtained at 140 K (Figure 2a) where the slope of the ρ−T curve changed. We note the similarity with the band Jahn−Teller effect or charge density wave, which often originates from the electronic instability inherent to a nested Fermi surface. One of the driving forces of the transition is the large DOS(E_F) value for HT YCu with a highly symmetrical structure,[34] which gives rise to the degeneracy of doubly degenerate Y 4d e_g (point 1 in Figure 3a) at the Γ point. However, it is difficult to apply such a concept to the phase transition of YCu because the structural relationship between the two polymorphisms is not connected by simple symmetry operations. Figure 4c shows the electron density map in the −7.0 eV to E_F energy region. The valence electron density shows the weak Cu−Cu zigzag chain along the b-axis. The Cu−Cu COHP (blue line) in Figure 3c also supports the existence of the bonding interaction in the −6.7 to −4.5 eV region. Differing from HT YCu, the Y−Y and Y−Cu COHPs are not optimized at E_F.

Phonon Structure. Figure 5a shows the phonon PDOS of LT and HT YCu calculated by the frozen phonon approach (the phonon band structure of HT YCu is given in Figure S5). No phonon mode has an imaginary frequency, confirming that these structures are dynamically stable at the ground states, which is consistent with the experimental result that HT YCu is stable even at low temperatures. For HT YCu, the features of the phonon DOS and band structure agree well with previously reported results.[35] The phonon band of HT YCu contains six bands attributable to the presence of two atoms in the ordered lattice of the bcc crystal structure. As can be seen in Figure S5, the lowest frequency optical mode of HT YCu is the doubly degenerate band at the M point (1.4 THz), whose vibration mode is in the closed-packing direction, <110>. Surprisingly, HT YCu with the smaller unit cell volume (i.e., the dense structure) has a lower maximum frequency (4.9 THz) than LT YCu with the larger unit cell volume of 5.4 THz, although it is usually expected that a denser solid has a higher phonon frequency. There is also another interesting feature of HT YCu; we can see that the heavy Y (red line) has a large contribution in the high-frequency (∼4.6 THz) phonon DOS, whereas the light Cu (blue line) has a large contribution in the low-frequency region (∼2.0 THz). These unexpected results can be understood by considering the crystal structure. In HT YCu, the low frequency of the Cu phonon DOS originates from the Cu ion loosely bound in it owing to the long d_{Cu-Y} (3.01 Å). The high-frequency Y-dominant modes originate from the rigid simple cubic (SC) framework of Y owing to the short d_{Y-Y} (3.47 Å), giving rise to a smaller unit cell volume. The maximum calculated phonon frequency is only 4.9 THz despite the strong Y−Y interaction, because Y is heavy. This is the origin of the unusual phonon behavior that the HT phase with high density has a lower maximum phonon frequency (4.9 THz) than the LT phase (5.4 THz). This unique Y−Y interaction can also be seen in the electron density map (Figure 1c) and the Y−Y COHP (Figure 3b). For LT YCu, we can see the comparable contributions of Y (red line) and Cu (blue line) in the phonon DOS in the high-frequency region (∼5.0 THz) (i.e., the unexpected features observed in HT YCu disappear). To confirm the softness of the Cu ions in the dense HT YCu structure, we investigated the energy potential surfaces of Cu at the Einstein approximation level (i.e., a Cu ion in 4a × 4b × 4c (HT) or 2a × 3b × 2c (LT) superlattice models is displaced along the <110> direction, which corresponds to the minimum-frequency optical mode at the M point in HT YCu). The calculated potential surfaces are shown in Figure S6 in the Supporting Information, and these indicate that HT YCu has a gentler potential curvature of the Cu ion than LT YCu does, confirming that the Cu ion is more loosely bound and vibrates in a larger region in HT YCu. Curve fitting using the equation $E(d) = E_0 + A_2 \times d^2 + A_4 \times d^4 + A_6 \times d^6$ shows the large contribution of the d^4 term in HT YCu, indicating that the light Cu ion is bound loosely in the Y-SC framework via the weak Y−Cu interaction. This reminds us that there is a rattling effect of phonon glasses in clathrate materials,[36] which is perhaps one of the origins of the soft phonon modes in the dense HT YCu. Figure 5b and 5c show the calculated constant-volume heat capacity (C_v), Helmholtz energy (F), and vibrational entropy (S_{vib}) for both the HT and LT YCu phases, respectively. These C_v curves converge to the Dulong−Petit value ($3R \times 2$) at ~300 K, whereas that of HT YCu rises steeply, reflecting the softening of the phonon structure. The difference between the Helmholtz energy of these phases at 0 K (i.e., the internal energy difference ΔF(0 K)) is only ~30 meV. The Helmholtz energy curves decrease as the temperature increases and gradually converge to cross at ~500 K, indicating a phase transition. Here, we should be aware of the possible error in the transition temperature. Usually, even for highly accurate DFT calculations, we should assume an error of ±10 meV per atom, which gives a corresponding error of the transition temperature of approximately ±150 K. These results are consistent with the experimental results, where the phase transition temperature has a wide ambiguity in the range of 140−550 K.[10] This calculation result confirms that the large vibrational entropy (Figure 5c) stabilizes the HT YCu structure at higher temperatures. The entropy ΔS for the phase transition at 500 K is estimated to be ~7 J mol^{-1} K^{-1} = $2 \times 0.4R$ (R: gas constant). We compare this value with those for similar phase transitions. For example, ΔS for a temperature-driven α−β phase transition of Sn at 286 K is $0.8R$[37] and ΔS for the melting of common metals is ~R according to Richard's rule. This comparison indicates that the phase transition of YCu is likely caused by a relatively small structural change.

Comparison with the Phase Transition of Sn. Finally, we briefly discuss the emergence of covalent bonding in YCu in comparison with the α−β phase transition of the metalloid Sn. Sn exhibits an allotropic α−β phase transition at T_{tr} = 286 K, which is one of the prototypes of the entropy-driven structural phase transition.[38] α-Sn (LT phase, gray tin) adopts a cubic diamond-type crystal structure. β-Sn (HT phase, white tin) takes a tetragonal diamond-type structure highly compressed along one of the three original cubic axes. The phase transition is driven by the formation of Sn−Sn covalent bonds through a metallic (HT)−covalent (LT) bond transition. The phase transition of Sn is understandable because Sn (with an electronegativity (EN) value of 1.72[39]) is located at the boundary between metallic and covalent element groups in the periodic table. By contrast, the average EN value (1.43) for YCu is close to that for V (1.45)[39] and is located in the metallic element region. In other words, the occurrence of covalent bonds in YCu is difficult to explain from the average EN value. Thus, we have proposed the emergence of covalent bonding in YCu from the perspective of chemical bonding. At low temperatures, the Y−Y and the Cu−Cu homolytic interactions play a critical role, inducing a less packed structure. In addition, the mixing enthalpy for Y/Cu, ΔH_{mix} = −22 kJ/mol,[40] indicates the capability of mixing in a solid. The negative ΔH_{mix} value means that Y and Cu have an attractive force between them, but the absolute value is not large. This gives rise to the competition of the Y−Cu, Y−Y, and Cu−Cu interactions in this compound at low temperatures. Thus, although the mixing of Y and Cu is possible at high temperatures with the aid of the entropy effect, it is not so easy at low temperatures.

■ CONCLUSION

Among the intermetallics, YCu is known to show a phase transition at 140−550 K, accompanied by NTE. This is an unusual material among intermetallics discovered so far in terms of its anomalous thermal expansion behavior without spin ordering. We reported on the experimental structure determination of the LT phase of YCu as well as the details of the phase transition, including the thermodynamics of the phase stability, which were obtained with the aid of DFT calculations. The results of this study are summarized as follows. (1) We synthesized a powder sample of ductile YCu by considering the ductile-brittle transition temperature. Structure refinements confirmed that the low-temperature phase adopts an FeB-type crystal structure. The structural changes for the FeB-type low-temperature phase were investigated at 300−723 K, confirming NTE behavior. (2) In this intermetallic, competition among the Y−Cu, Y−Y, and Cu−Cu interactions exists. The mixing of Y and Cu is difficult at low temperatures owing to the weak attractive force between these atoms. At low temperatures, the Y−Y and Cu−Cu covalent interactions induce segregation in the FeB-type crystal structure, where internal energy is dominant in the Helmholtz energy. (3) At higher temperatures, Cu ions are loosely bound to Y ions owing to the long Y−Cu distance (3.01 Å), and the large vibration entropy stabilizes the CsCl-type structure. Furthermore, the Y−Y interaction between neighboring unit cells reinforces the simple cubic sublattice of Y to realize a smaller unit cell volume. The role of the Y−Y interaction is supported by the calculated high-frequency phonon DOS of Y (~4.9 THz). The high-temperature phase has the simple cubic framework of Y containing a Cu ion bound loosely in the cavity site.

■ ASSOCIATED CONTENT

Ⓢ Supporting Information

The Supporting Information is available free of charge on the ACS Publications website at DOI: 10.1021/acs.inorgchem.9b01988.

> Crystal structure parameters and structural features for LnCu (Ln = La, Ce, Pr, Nd, Sm, and Y); powder XRD patterns for LnCu (Ln = La, Ce, Pr, Nd, Sm, and Y); temperature dependence of the unit cell volume of HT and LT YCu; projected DOS for HT YCu; band structure for LT YCu; calculated phonon dispersion curves of HT YCu and Cu potential surfaces for HT and LT YCu (PDF)

Accession Codes

CCDC 1891439−1891441, 1898819, 1905378, and 1937824 contain the supplementary crystallographic data for this paper. These data can be obtained free of charge via www.ccdc.cam.ac.uk/data_request/cif, or by emailing data_request@ccdc.cam.ac.uk, or by contacting The Cambridge Crystallographic Data Centre, 12 Union Road, Cambridge CB2 1EZ, UK; fax: +44 1223 336033.

■ AUTHOR INFORMATION

Corresponding Authors

*E-mail: hosono@mces.titech.ac.jp. (H.H.)
*E-mail: mizoguchi@mces.titech.ac.jp. (H.M.)

ORCID

Hiroshi Mizoguchi: 0000-0002-0992-7449
Hideo Hosono: 0000-0001-9260-6728

Author Contributions

§H.M. and J.B. contributed equally.

Notes

The authors declare no competing financial interest.

■ ACKNOWLEDGMENTS

This study was supported by the MEXT Element Strategy Initiative to form Core Research Centers. We thank Sang-Won Park (Tokyo Institute of Technology) for help in the DFT calculations. We also thank Dr. N. S. P. Bhuvanesh (Texas A&M University) for help in the structure refinements. H.M. was also supported by the JSPS through a Grant-in-Aid for Scientific Research (18K05270).

■ REFERENCES

(1) (a) Sleight, A. W. Compounds That Contract on Heating. *Inorg. Chem.* **1998**, *37*, 2854−2860. (b) Takenaka, K. Negative thermal expansion materials: technological key for control of thermal expansion. *Sci. Technol. Adv. Mater.* **2012**, *13*, 013001/1-11.

(2) Zener, C. Impact of magnetism upon metallurgy. *JOM* **1955**, 7 (5), 619−630.

(3) *Magnetic, Electrical, and Optical Properties and Applications of Intermetallic Compounds*, Westbrook, J. H.; Fleischer, R. L., Eds.; Wiley: New York, 2000.

(4) For examples, see: (a) Lee, S.; Hoffmann, R. Bcc and Fcc Transition Metals and Alloys: A Central Role for the Jahn-Teller Effect in Explaining Their Ideal and Distorted Structures. *J. Am. Chem. Soc.* **2002**, *124*, 4811−4823. (b) Lin, Q.; Corbett, J. D. A chemical approach to the discovery of quasicrystals and their approximant crystals. *Struct. Bonding* **2009**, *133*, 1−39. (c) Wang, F.; Miller, G. J. Revisiting the Zintl-Klemm Concept: Alkali Metal Trielides. *Inorg. Chem.* **2011**, *50*, 7625−7636. (d) Vinokur, A.; Fredrickson, D. 18-Electron Resonance Structures in the BCC Transition Metals and Their CsCl-type Derivatives. *Inorg. Chem.* **2017**, *56*, 2834−2842. (e) Mizoguchi, H.; Muraba, Y.; Fredrickson, D.; Matsuishi, S.; Kamiya, T.; Hosono, H. The Unique Electronic Structure of Mg_2Si: Shaping the Conduction Bands of Semiconductors with Multicenter Bonding. *Angew. Chem., Int. Ed.* **2017**, *56*, 10135−10139. (f) Park, S.-W.; Hosono, H.; Fredrickson, D. Cation Clustering in Intermetallics: The Modular Bonding Schemes of CaCu and Ca_2Cu. *Inorg. Chem.* **2019**, *58*, 10313−10322.

(5) Hartjes, K.; Jeitschko, W. Crystal structures and magnetic properties of the lanthanoid nickel antimonides LnNiSb (Ln = La-Nd, Sm, Gd-Tm, Lu). *J. Alloys Compd.* **1995**, *226*, 81−86.

(6) Mishra, R.; Pottgen, R.; Hoffmann, R.-D.; Fickenscher, T.; Eschen, M.; Trill, H.; Mosel, B. Ternary antimonides YbTSb (T = Ni, Pd, Pt, Cu, Ag, Au) - synthesis, structure, homogeneity ranges, and ^{121}Sb Mossbauer spectroscopy. *Z. Naturforsch., B: J. Chem. Sci.* **2002**, *57*, 1215−1223.

(7) Ackerbauer, S.; Senyshyn, A.; Borrmann, H.; Burkhardt, U.; Ormeci, A.; Rosner, H.; Schnelle, W.; Gamza, M.; Gumeniuk, R.; Ramlau, R.; Bischoff, E.; Schuster, J.; Weitzer, F.; Leithe-Jasper, A.; Tjeng, L.; Grin, Y. Structural transformation with "negative volume expansion": chemical bonding and physical behavior of TiGePt. *Chem. - Eur. J.* **2012**, *18*, 6272−6283.

(8) Song, Y.; Chen, J.; Liu, X.; Wang, C.; Zhang, J.; Liu, H.; Zhu, H.; Hu, L.; Lin, K.; Zhang, S.; Xing, X. Zero Thermal Expansion in Magnetic and Metallic $Tb(Co,Fe)_2$ Intermetallic Compounds. *J. Am. Chem. Soc.* **2018**, *140*, 602−605.

(9) Van Dongen, J.; Palstra, T.; Morgownik, A.; Mydosh, J.; Geerken, B.; Buschow, K. H. J. Crystal-structure transformations and magnetic-ordering phenomena in $GdCu_{1-x}Ga_x$. *Phys. Rev. B: Condens. Matter Mater. Phys.* **1983**, *27*, 1887−1902.

(10) (a) Kadomatsu, H.; Kawanishi, Y.; Kurisu, M.; Tokunaga, T.; Fujiwara, H. Structural phase transitions in $YCu_{1-x}M_x$ (M = Ni, Ag and Ga). *J. Less-Common Met.* **1988**, *141*, 29−36. (b) Ibarra, M.R.; Chien, T.S.; Pavlovic, A.S. Structural instability in RCu intermetallic compounds. *J. Less-Common Met.* **1989**, *153*, 233−243.

(11) (a) Morris, J.; Ye, Y.; Lee, Y.; Harmon, B.; Gschneidner, K., Jr.; Russell, A. Ab initio calculation of bulk and defect properties of ductile rare-earth intermetallic compounds. *Acta Mater.* **2004**, *52*, 4849−4857. (b) Shi, Y.; Du, Y.; Chen, G.; Chen, G. L. First principle study on phase stability and electronic structure of YCu. *Phys. Lett. A* **2007**, *368*, 495−498.

(12) Li, C.; Yu, Z.; Lu, T.; Liu, H. Structural stability of intermetallic compound YCu studied by ab initio total energy calculation. *Phys. B* **2012**, *407*, 3916−3919.

(13) Ritter, C.; Ibarra, M. R.; Ibberson, R. The low temperature orthorhombic structure of YCu. *J. Phys.: Condens. Matter* **1993**, *5* (4), L39−L42.

(14) Cahn, R. W. Intermetallics: New physics. *Contemp. Phys.* **2001**, *42*, 365−375.

(15) Gschneidner, K., Jr.; Russell, A.; Pecharsky, A.; Morris, J.; Zhang, Z.; Lograsso, T.; Hsu, D.; Chester Lo, C. H.; Ye, Y.; Slager, A.; Kesse, D. A family of ductile intermetallic compounds. *Nat. Mater.* **2003**, *2*, 587−590.

(16) For examples, see: (a) Zhang, Z.; Russell, A.; Biner, S.; Gschneidner, K., Jr.; Lo, C. Fracture toughness of polycrystalline YCu, DyCu, and YAg. *Intermetallics* **2005**, *13*, 559−564. (b) Oertel, C.; Schaarschuch, R.; Cao, G.; Tian, H.; Freudenberger, J.; Brokmeier, H.; Skrotzki, W. Effect of martensitic phase transformation on the ductility of polycrystalline YCu. *Scr. Mater.* **2011**, *65*, 779−782.

(17) TOPAS, Version 4.2, Bruker AXS: Karlsruhe, Germany, 2009.

(18) (a) Perdew, J. P.; Burke, K.; Ernzerhof, M. Generalized Gradient Approximation Made Simple. *Phys. Rev. Lett.* **1996**, *77*, 3865−3868. (b) Blöchl, P. E. Projector augmented-wave method. *Phys. Rev. B: Condens. Matter Mater. Phys.* **1994**, *50*, 17953−17979. (c) Kresse, G.; Furthmüller, J. Efficient iterative schemes for ab initio total-energy calculations using a plane-wave basis set. *Phys. Rev. B: Condens. Matter Mater. Phys.* **1996**, *54*, 11169−11186.

(19) Deringer, V.; Tchougreeff, A.; Dronskowski, R. Crystal Orbital Hamilton Popilation (COHP) Analysis as Projected from Plane-Wave Basis Sets. *J. Phys. Chem. A* **2011**, *115*, 5461−5466.

(20) Sanville, E.; Kenny, S.; Smith, R.; Henkelman, G. Improved grid-based algorithm for Bader charge allocation. *J. Comput. Chem.* **2007**, *28*, 899−908.

(21) Momma, K.; Izumi, F. VESTA 3 for three-dimensional visualization of crystal, volumetric and morphology data. *J. Appl. Crystallogr.* **2011**, *44*, 1272−1276.

(22) Mei, Z.; Shang, S.; Wang, Y.; Liu, Z. Density-functional study of the thermodynamic properties and the pressure−temperature phase diagram of Ti. *Phys. Rev. B: Condens. Matter Mater. Phys.* **2009**, *80*, 104116/1-9.

(23) Togo, A.; Tanaka, I. First principles phonon calculations in materials science. *Scr. Mater.* **2015**, *108*, 1−5.

(24) Chao, C.; Luo, H.; Duwez, P. CsCl-Type Compounds in Binary Alloys of Rare-Earth Metals with Zinc and Copper. *J. Appl. Phys.* **1964**, *35*, 257−258.

(25) Swanson, H. E. Standard x-ray diffraction powder patterns. *Nat. Bureau Stand. Circular* **1953**, *539*, 1−95.

(26) Buschow, K. H. J.; Van Vucht, J.; Van Den Hoogenhof, W. The crystal structures of Eu_3Ag_2, EuAg and EuCu. *J. Less-Common Met.* **1980**, *75*, P17−P22.

(27) Belan, B.; Bodak, O.; Cerny, R.; Pacheco, J.; Yvon, K. Crystal structure of ytterbium copper, YbCu. *Z. Kristallogr. - New Cryst. Struct.* **1997**, *212*, 508.

(28) Balster, H.; Ihrig, H.; Kockel, A.; Methfessel, S. Martensitic crystal structure transformation in CsCl-type alloys YCu, LaCd, and $LaAg_xIn_{1-x}$. *Z. Phys. B: Condens. Matter Quanta* **1975**, *21*, 241−245.

(29) Otsuka, K.; Ohba, T.; Tokonami, M.; Wayman, C. New description of long period stacking order structures of martensites in β-phase alloys. *Scr. Metall. Mater.* **1993**, *29*, 1359−1364.

(30) Chaboy, J.; Ibarra, M. R. X-ray-absorption spectroscopy investigation of the martensitic structural transformation in the RCu (R = rare earth) series. *Phys. Rev. B: Condens. Matter Mater. Phys.* **1995**, *52*, 3206−3213.

(31) Gschneidner, K., Jr.; Ji, M.; Wang, C.; Ho, K.; Russell, A.; Mudryk, Y.; Becker, A.; Larson, J. L. Influence of the electronic structure on the ductile behavior of B2 CsCl-type AB intermetallics. *Acta Mater.* **2009**, *57*, 5876−5881.

(32) Spedding, F.; Daane, A.; Herrmann, K. The crystal structures and lattice parameters of high-purity scandium, yttrium, and the rare earth metals. *Acta Crystallogr.* **1956**, *9*, 559−563.

(33) Hoffmann, R. How Chemistry and Physics Meet in the Solid State. *Angew. Chem., Int. Ed. Engl.* **1987**, *26*, 846−878.

(34) Ghatak, S.; Ray, D.; Tannous, C. Studies of the structural stability of an electronic system with a two-fold degenerate band. *Phys. Rev. B: Condens. Matter Mater. Phys.* **1978**, *18*, 5379−5384.

(35) Wang, R.; Wang, S.; Wu, X.; Liu, A. First-principles phonon calculations of thermodynamic properties for ductile rare-earth intermetallic compounds. *Intermetallics* **2011**, *19*, 1599−1604.

(36) Sales, B.; Mandrus, D.; Chakoumakos, B.; Keppens, V.; Thompson, J. Filled skutterudite antimonides: Electron crystals and phonon glasses. *Phys. Rev. B: Condens. Matter Mater. Phys.* **1997**, *56*, 15081−15089.

(37) (a) Ihm, J.; Cohen, M. L. Equilibrium properties and the phase transition of grey and white tin. *Phys. Rev. B: Condens. Matter Mater. Phys.* **1981**, *23*, 1576−1579. (b) Pavone, P.; Baroni, S.; de Gironcoli, S. $\alpha \leftrightarrow \beta$ phase transition in tin: A theoretical study based on density-functional perturbation theory. *Phys. Rev. B: Condens. Matter Mater. Phys.* **1998**, *57*, 10421−10423.

(38) Musgrave, M. On the relation between grey and white tin (α-Sn and β-Sn). *Proc. R. Soc. London, A* **1963**, *272*, 503−528.

(39) Allred, A.; Rochow, E. A scale of electronegativity based on electrostatic force. *J. Inorg. Nucl. Chem.* **1958**, *5*, 264−268.

(40) Takeuchi, A.; Inoue, A. Classification of Bulk Metallic Glasses by Atomic Size Difference, Heat of Mixing and Period of Constituent Elements and Its Application to Characterization of the Main Alloying Element. *Mater. Trans.* **2005**, *46*, 2817−2829.